Proceedings of the ASME 2024 19th International Manufacturing Science and Engineering Conference
MSEC2024
June 17-21, 2024, Knoxville, Tennessee

MSEC2024-124411

EMBEDDED FUSED DEPOSITION MODELING OF PCL ORBITAL IMPLANTS WITH ENHANCED PERFORMANCE

Kellen Mitchell, Aidan Shackleford, Erick Bandala, Yifei Jin
Department of Mechanical Engineering, University of Nevada, Reno
Reno, NV, USA

Guangrui Cha
Department of Ophthalmology, Shengjing Hospital of China Medical University
Shenyang, Liaoning, China

ABSTRACT

Orbital implants are necessary for reconstructing fractured orbital walls and are traditionally fabricated using titanium or polyethylene, but these materials result in medical complications such as increased risk of implant migration and hemorrhaging. Therefore, orbital implants constructed from biocompatible and biodegradable polymers have been recently researched to mitigate these risks. Material extrusion three-dimensional (3D) printing techniques, especially fused deposition modeling (FDM), can be applied to produce patient-specific orbital implants. However, current structures fabricated by FDM usually possess poor mechanical properties and high surface roughness. In this work, an embedded FDM method is designed and implemented to fabricate polycaprolactone (PCL) orbital implants with increased mechanical properties and surface morphology through the development and utilization of a temperature-stable yield-stress suspension comprised of fumed silica particles and a sunflower oil solvent. The rheological properties of the suspension were measured and tuned to produce a viable support bath material above the melting temperature of PCL. Filaments, single-layer sheets, and tensile test samples were printed to optimize the printing parameters, verify the surface morphology, and validate the mechanical properties, respectively. After that, a numerical simulation was performed to determine the mechanical robustness of the designed orbital implant model. Finally, the orbital implant was printed, measured, and implanted into a mock-up orbital socket to verify the viability of the proposed embedded FDM method.

Keywords: embedded 3D printing, orbital implant, sunflower oil, fumed silica, yield-stress fluid, polycaprolactone

1. INTRODUCTION

Due to the increase in traffic, workplace, and sports accidents, orbital bone fractures have risen in recent years. For patients suffering from orbital bone fractures, orbital implants may be necessary for a complete recovery [1, 2]. Contemporary orbital implants are primarily produced from titanium [1, 3, 4] and polyethylene [1, 5, 6], which are manufactured into a generalized geometry such that they can be further bent and/or trimmed to fit the patient's orbital shape [7]. As common as these implants are, titanium and polyethylene materials present certain challenges post-implantation. Titanium and polyethylene are characterized as nonabsorbable implants and, therefore, are not degraded by the patient's body, which commonly leads to negative effects such as infection, delayed inflammation, hemorrhaging, and implant migration [8, 9]. If these complications are severe, secondary procedures may be necessary, which increases patient risk.

Biocompatible and biodegradable thermoplastic polymer materials, such as polylactic acid (PLA), polyglycolic acid (PGA), and polycaprolactone (PCL), have demonstrated potential as bone implants and do not cause the severity of side effects as nonabsorbable implants [8-10]. The good biocompatibility of these materials results in a relatively small immune response compared to traditional, nonabsorbable materials. Because the implant slowly degrades, the patient's bone is allowed to grow and replace the implant to permanently heal the fracture [11]. In addition, these materials can be easily and rapidly manufactured through three-dimensional (3D) printing techniques to produce patient-specific orbital bone implants [8, 12-15]. Despite their advantages, certain biodegradable thermoplastics pose a health risk during degradation. For example, PLA and PGA degrade rapidly, which may result in contour and structural loss before proper bone growth can occur. Additionally, PLA and PGA can produce an inflammatory response in the surrounding tissue caused by acidic metabolites following degradation [8]. On the other hand, PCL degrades at a much slower rate and does not produce harmful byproducts, making it a more suitable material for 3D-printed orbital implants [8, 10].

In recent studies, PCL orbital implants produced through fused deposition modeling (FDM), a material extrusion 3D printing technique, have shown promise [8, 14]. FDM printing selectively deposits molten thermoplastic filaments layer-by-layer through a heated printhead onto a substrate or previously printed layers at a low ambient temperature to form 3D structures, as shown in Fig. 1a [16, 17]. FDM printing provides a method for the rapid fabrication of patient-specific implants

that cannot be manufactured using traditional techniques. Despite its advantages, FDM 3D printing presents inherent challenges regarding mechanical properties and surface characteristics. For example, the rapid cooling of deposited filaments produces the necessary mechanical properties for shape retention and support for the following layers. However, it also leads to poor intra- and interlayer adhesion, resulting in poor mechanical properties [18, 19]. Additionally, filaments printed using FDM must be spaced with minimal filament overlap to reduce printhead clogging and interference, which also reduces intralayer adhesion and increases the surface roughness of the structure (inset of Fig. 1a) [16, 20, 21]. Embedded ink writing (EIW), another material extrusion 3D printing technique, can potentially control the ambient temperature of deposited inks to improve the mechanical properties and surface morphology of PCL orbital implants. In EIW, inks are deposited through a printhead/nozzle into a support bath to fabricate 3D structures. The support bath can hold the printed structures *in situ* in a liquid state, which promotes intra- and interlayer filament fusion [22, 23]. However, current EIW techniques commonly print ink materials at low temperatures (e.g., room temperature), which are much lower than the melting points of thermoplastics. The utilized support baths are usually aqueous-based and cannot withstand the high temperatures required to hold thermoplastics at a molten state [22, 24, 25]. Oil-based support baths with higher temperature stability have been utilized for EIW printing [26, 27]. Like their aqueous counterparts, these bath materials are used to support inks at room temperature. Then, the support bath is heated to crosslink or sinter the printed inks to form homogeneous structures [26, 27]. Because of the material and process restrictions required of current EIW techniques, thermoplastic materials cannot be printed using this strategy to produce structures with increased mechanical properties and surface morphologies without complex post-treatment steps. Therefore, an advanced FDM printing technique is necessary to produce PCL orbital implants with elevated mechanical and surface characteristics to better suit patients suffering from orbital bone fractures.

Herein, an embedded FDM (e-FDM) printing technique has been developed to fabricate thermoplastic structures with

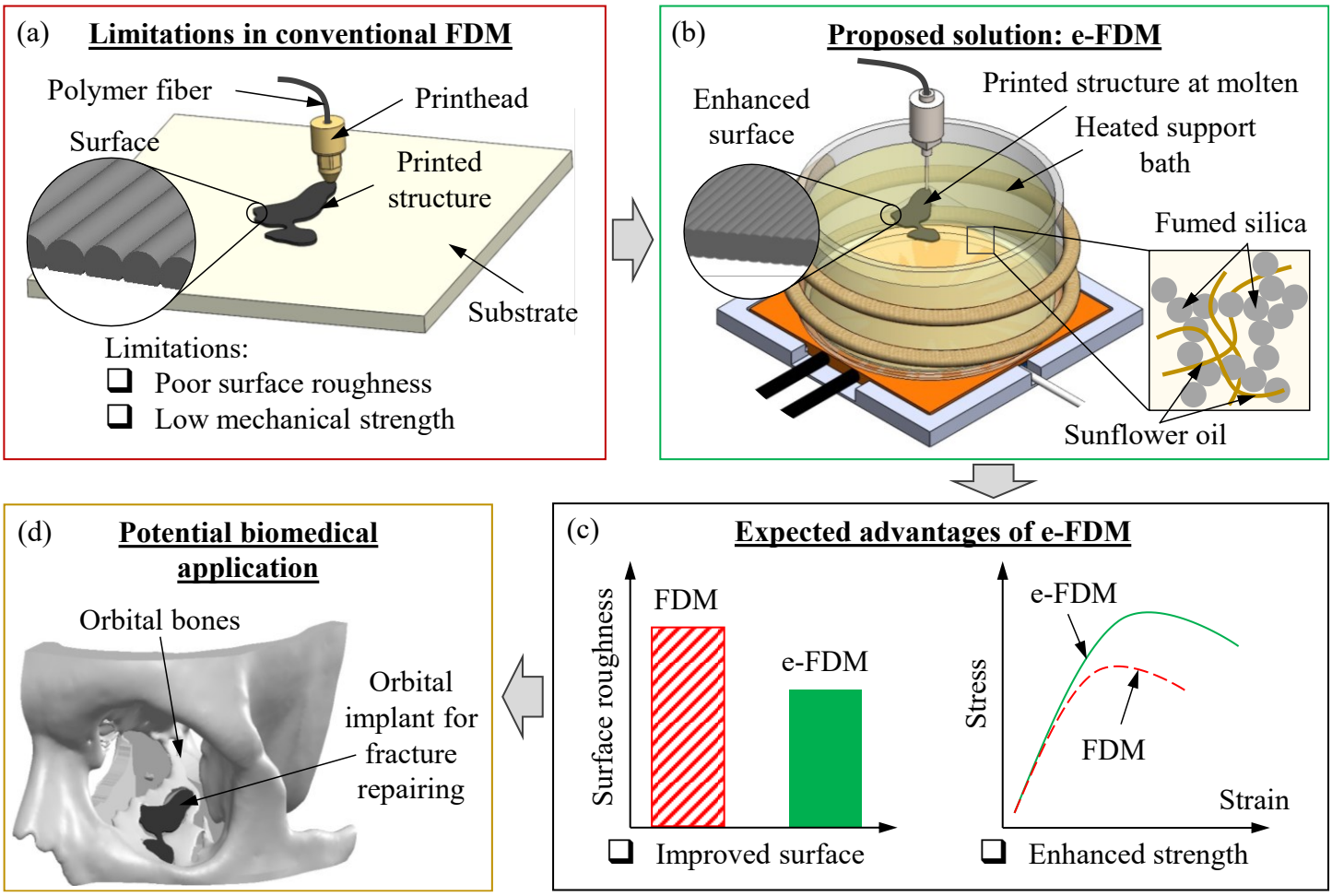

FIGURE 1: (A) OVERVIEW AND LIMITATIONS OF FDM 3D PRINTING. (B) PROPOSED E-FDM 3D PRINTING METHOD UTILIZING A HEATED SUPPORT BATH AND A THERMOSTABLE FUMED SILICA-SUNFLOWER OIL SUSPENSION TO PRINT THERMOPLASTIC STRUCTURES. (C) THE EXPECTED OUTCOMES AND ADVANTAGES OF E-FDM PRINTING OVER FDM PRINTING. (D) A POTENTIAL BIOMEDICAL APPLICATION OF A PCL ORBITAL IMPLANT PRODUCED VIA E-FDM PRINTING.

enhanced mechanical properties and surface roughness to produce patient-specific PCL orbital implants, as depicted in Fig. 1b. To establish this technique, a thermostable support bath comprised of fumed silica (FS) and sunflower oil (SFO) was designed through rheological testing to support the PCL filament above the thermoplastic's melting point throughout the duration of the printing process. Then, printing tests were conducted to find suitable printing conditions. Next, single-layer sheets and dog bone tensile samples were produced using FDM and e-FDM to confirm that e-FDM can produce structures with increased surface morphologies and mechanical properties (Fig. 1c). An exemplary orbital implant was then designed and verified to possess the necessary mechanical robustness to support an eyeball and its surrounding tissue through numerical structural simulation. Lastly, an orbital implant was printed, measured, and implanted into a model skull, as shown in Fig. 1d, to prove the viability of the e-FDM printing technique.

2. MATERIALS AND METHODS

2.1 Support Bath Preparation and Characterization

An appropriate amount of FS (Aerosil R812S, Evonik, Vernon, CA) was dispersed in an SFO purchased from a local provider (Raley's, Reno, NV). Then, the FS-SFO mixture was stirred at 300 RPM for 5 minutes using an overhead stirrer (LACHOI LCH-OES-20L, Shaoxing, China). After mixing, the FS-SFO suspension was degassed using a centrifuge (Cole-Palmer VS3400, Antylia Scientific, Vernon Hills, IL) for 3 minutes at 2500 rpm to remove entrapped air bubbles. All bath material preparations were conducted at room temperature. To investigate the effects of FS concentration on the rheological properties, 8.0, 10.0, and 12.0% (w/w) FS-SFO suspensions were produced and tested. All three concentrations of FS-SFO suspensions were subjected to temperature sweep and shear rate sweep rheological testing using a rheometer (MCR 92, Anton Paar, Gratz, Austria).

Temperature sweeps were conducted using a parallel plate tool and a tool gap of 1.000 mm. During testing, the frequency and strain amplitude were held constant at 1 Hz and 1%, respectively, and the temperature was increased from 30 ℃ to 100 ℃. Shear rate sweep rheological tests were conducted using a conical plate at a tool gap of 0.100 mm. During testing, the rheometer was held at a constant temperature of 85 ℃ while the shear rate increased from 0.01 to 1000 s^{-1}.

2.2 Printing System and Printing Procedures

Printing system. A modified FDM 3D printer (Ender3 Pro, Creality, Shenzhen, China) was utilized to print 1.75 mm diameter PCL filament (Uxcell, Hongkong, China). Printer modifications include stainless-steel blunt tip luer lock nozzles and a heated support bath assembly. 18-, 20-, and 22-gauge nozzles (Harfinton, Hongkong, China), all 0.5 inches in length, were attached to the printhead and utilized to dispense the PCL filament into the heated support bath. The heated support bath assembly consists of an 80 mm diameter by 40 mm glass crystallizing dish (PYREX, Rosemont, IL), silicone rubber heating blanket (SRW030-030A010A00-UR, BriskHeat, Columbus, OH), cord heater (HTC451001, BriskHeat, Columbus, OH) and two heat controllers (SDXRA, BriskHeat, Columbus, OH). The base and walls of the crystallizing dish are heated by the silicone rubber heating blanket and the cord heater, respectively. The crystallizing dish and both heaters are positioned on top of the print bed of the FDM printer and held in place by an aluminum and PLA fixture fabricated by the mechanical engineering machine shop at the University of Nevada, Reno.

Printing procedures. For all e-FDM printing, 90 g of 12% (w/w) FS-SFO is added to the crystallizing dish and used as the support bath material. Before printing, the bath is heated to an average temperature of 85 ℃ for 45 minutes to ensure a thoroughly heated support bath. A printhead temperature of 90 ℃ and print speed of 0.5 mm/s is also consistent for all printing procedures. Single filaments, single-layer sheets, dog bone tensile samples, and orbital implants were all printed using the PCL filament. Besides the single filaments, all prints utilized a 20-gauge nozzle size and an extrusion flow rate of 0.52 mm^3/s. Single-layer sheets and dog bone tensile samples were also printed using a traditional FDM printer (CR-10 v3, Creality, Shenzhen, China) utilizing a 0.600 mm inner diameter printhead, 90 ℃ printhead temperature, 30 ℃ substrate temperature, 0.5 mm/s print speed, 0.4 mm layer height, and overlap ratio of 125%.

The single filaments are printed to be 20 mm long using various flow rates and nozzle gauges. First, filaments were printed at extrusion flow rates of 0.23, 0.52, and 0.93 mm^3/s using a 20-gauge nozzle. Second, 18-, 20-, and 22-gauge nozzles were used to print filaments at a constant flow rate of 0.52 mm^3/s.

10 mm by 5 mm single-layer PCL sheets were designed using SolidWorks 2023 (Dassault Systèmes, Vélizy-Villacoublay, France) computer-aided design (CAD) software, sliced using Cura 5.3.1 (UltiMaker, Utrecht, Netherlands) and printed using e-FDM with multiple overlap ratios. The overlap ratio is defined as the ratio of the distance between adjacent filament centerlines to the filament diameter. In the case of this work, the single-layer sheets were printed with overlap ratios of 30%, 40%, and 50%.

The dog bone tensile samples printed utilizing FDM and e-FDM were a single layer thick. The dog bone samples were also printed with a 0-degree raster angle so that the inter-filament interfaces are perpendicular to the tensile strain direction. Additionally, the e-FDM dog bone samples were printed using a 40% overlap ratio. The PCL orbital implant was produced using printing parameters identical to the e-FDM dog bone tensile samples.

Post-printing procedure. Once printing was finished, the support bath was left to cool to room temperature for all printed structures. Then, the printed structure was removed from the bath, excess bath material was gently wiped off the structure, and the structure was soaked in a 25% (v/v) soap-water mixture for 1 hour to remove the remaining bath material using Dawn dish soap (Procter & Gamble, Cincinnati, OH). The wiping and soaking steps were repeated as necessary.

2.3 Filament and Surface Roughness Characterization

The diameters of the single filaments printed using various extrusion flow rates and nozzle gauges were measured using digital calipers (Neiko, Wenzhou, China). The resulting diameters of the filaments are used to determine the filament geometry controllability and the parameters used in subsequent printing procedures.

The root-mean-square (RMS) surface roughness, R_{RMS}, of the single-layer sheets printed via e-FDM and FDM was measured using a microscope (Vertex 251 UC, Micro-Vu, Windsor, CA) and InSpec 1.2.0 measurement software (Micro-Vu, Windsor, CA). The R_{RMS} values are used to determine the surface morphology of the printed structures.

2.4 Mechanical Property Measurement

Dog bone tensile samples with a 0-degree raster angle were printed using e-FDM and FDM printing techniques. After printing, the length, width, and thickness of the reduced section of the tensile samples were measured using digital calipers, and the cross-sectional areas were calculated. Tensile tests were performed for dog bone samples using an ADMET 7600 mechanical property tester (ADMET, Norwood, MA) to determine the PCL printed structures' ultimate strength and ultimate strain using both techniques.

2.5 Orbital Implant Structural Simulation

An exemplary CAD model of a skull possessing a fractured orbital bone and a two-dimensional orbital implant was created using SolidWorks 2023. The orbital patch has a designed height, width, and thickness of 27.05, 16.07, and 1.25 mm, respectively. A numerical structural simulation of the orbital implant model was performed using ANSYS AIM 19.2 (Canonsburg, PA), where the outer edge of the orbital implant possessed a fixed geometry and a normal load of 35 g acting vertically on the flat surface of the implant to simulate the weight of the eyeball and surrounding tissue. Material properties, such as density and Poisson's ratio, ultimate stress, and ultimate strain, were obtained from literature, and the mechanical properties obtained from mechanical testing were used as the material properties of PCL within the simulation to determine the structural robustness of the orbital implant.

2.6 Orbital Implant Shape Fidelity and Installation

An e-FDM printed orbital implant and a skull possessing an orbital fracture were used to show the viability of the PCL orbital implant. After printing the orbital implant, the height, width, and thickness were measured and compared to the respective values of the orbital implant CAD model. Then, the exemplary skull model was sliced and printed on an FDM printer using a PLA filament, and the PCL orbital implant was installed into the fracture site of the orbital socket.

2.7 Statistical Analysis

All experiments, including rheological testing, filament and structure printing, surface roughness measurement, and mechanical property testing, were repeated three times in this work, and the quantitative values are reported as means ± standard deviations.

3. RESULTS AND DISCUSSION

3.1 Support Bath Selection and Rheological Characterization

The proposed e-FDM 3D printing method utilizes a support bath to hold deposited molten filaments *in situ*; therefore, certain rheological properties are required for printing. Like the proposed method, EIW utilizes a support bath, typically comprised of a thixotropic particle additive and an aqueous or polymer solvent, to hold liquid inks during printing [22, 27, 28]. To effectively hold filaments and allow for the nozzle/printhead to translate within the bath, the support bath material must possess a yield-stress property, where the support bath material acts solid-like below the yield stress and as a liquid when above. With a yield-stress property, the bath material will be able to flow around the nozzle during translation and convert back to solid-like to support the deposited filament. A suitable yield stress range between 10 and 550 Pa has been determined experimentally for EIW support bath materials [29, 30]. Whether a low or high yield stress is selected for a printing application depends on the support bath and ink material properties as well as printing parameters, such as print speed [29, 31, 32]. In the case of printing thermoplastic inks, the ambient temperature of the support bath must be above the melting point of the thermoplastic material. Therefore, the selected bath material must be thermostable and possess a yield stress above the melting point of the thermoplastic filament to produce a viable support bath for the proposed e-FDM technique. For the PCL filament selected in this work, the melting point generally occurs between 56 and 65 °C [33]. In addition to possessing suitable rheological properties, the hydrophobicity of the support bath will also affect the proposed printing method. PCL is hydrophobic and, therefore, better suited to be printed into a hydrophobic bath to reduce surface tension between the bath material and the molten filament [34]. If an ink/filament were to be printed into a bath of opposite hydrophobicity, the potential for discontinuous filaments and structures would be greatly increased [23]. Herein, an oil-based yield-stress fluid comprised of an SFO solvent and FS thixotropic additive is selected as the support bath for the proposed e-FDM printing. SFO possesses a high smoking point of 220 °C and is highly hydrophobic, making it stable at high temperatures and compatible with hydrophobic inks [35]. Additionally, dispersing FS in certain concentrations converts the suspension into a yield-stress fluid with tunable rheological properties, making this suspension an ideal support bath material for e-FDM [36, 37].

To analyze the functionality of the support bath material and to find an optimal FS concentration, 8%, 10%, and 12% (w/w) FS-SFO suspensions were subjected to temperature sweep and shear rate sweep rheological tests. The temperature sweep data in Fig. 2a depicts a constant and stable storage modulus (G') for the three concentrations, resulting in thermostable suspensions

for all tested concentrations. Additionally, *G'* increases with FS concentration at all measured temperatures, indicating an increase in elasticity when higher concentrations of FS are dispersed in SFO.

Then, shear rate sweep tests at an elevated temperature of 85 °C are applied to characterize the yield stress of the suspensions by fitting the resulting shear stress data to the Hershel-Bulkley model:

$$\tau = \tau_0 + k\dot{\gamma}^n \quad (1)$$

where τ is the shear stress, τ_0 is the yield stress, k is the consistency index, $\dot{\gamma}$ is the shear rate, and n is the flow index. Through preliminary printing tests, an average support bath temperature of 85 °C was deemed necessary for printing PCL filaments. Figure 2b illustrates that the shear stress increases with the shear rate for all three concentrations of FS. By fitting the measured shear stress values to Eq. (1), the yield stress for the concentrations was calculated. It was determined that all three concentrations of the FS-SFO suspension presented as yield-stress fluids at 85 °C, with yield stress values increasing with FS concentration and ranging from 3.68 ± 0.14 Pa to 17.4 ± 1.75 Pa.

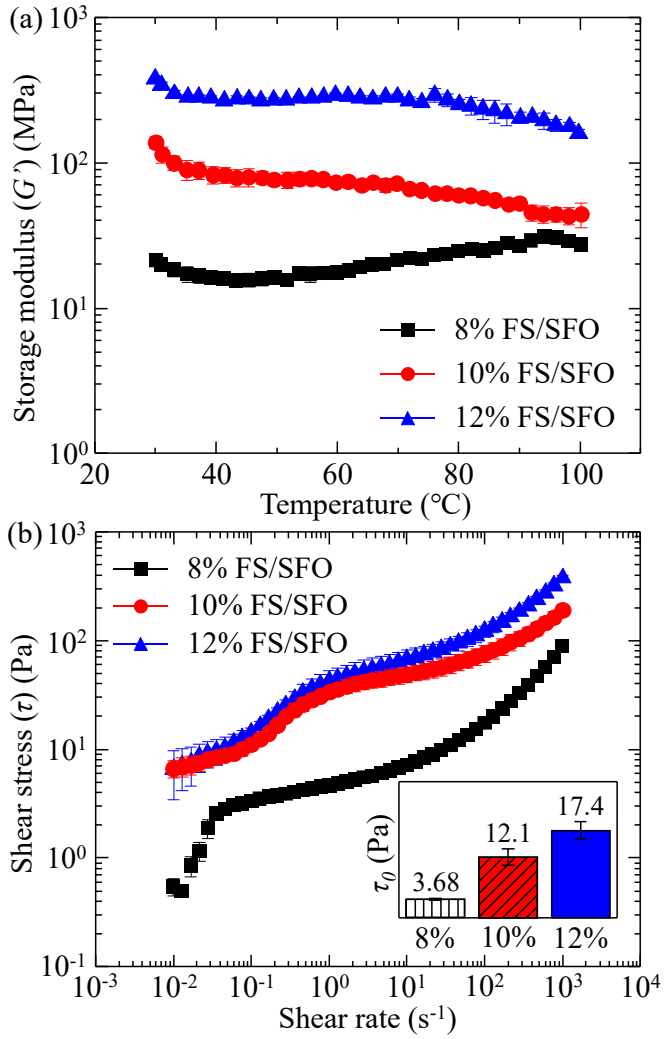

FIGURE 2: RHEOLOGICAL PROPERTIES OF FS-SFO SUSPENSIONS WITH DIFFERENT FUMED SILICA CONCENTRATIONS. (A) STORAGE MODULUS AS A FUNCTION OF TEMPERATURE. (B) SHEAR STRESS AS A FUNCTION OF SHEAR RATE AT 85 °C.

The increase in *G'* and yield stress is directly attributed to the increase in FS concentration and the creation of denser 3D networks within the suspension. FS particles form aggregates and aggregate chains, which form a volume-filling network that entraps and entangles the SFO polymer chains (Fig 1b), resulting in a yield-stress fluid. An increase in FS concentration increases the aggregate and aggregate chain density as well as the SFO polymer entanglements, producing a more elastic structure that requires larger shear stress to cause the fluid to flow [26, 36, 38]. Additionally, the yield stress values found at these concentrations and temperatures are similar to those found when rheological testing is conducted at room temperature, indicating that temperature does not significantly affect yield stress in this temperature scale [26, 27].

The performed rheological tests proved that all three concentrations are thermostable yield-stress fluids in the desired temperature region. Furthermore, two of three concentrations (10% and 12%) produce yield stresses in the necessary range for viable support bath materials. Both concentrations may be viable for e-FDM, but the increased *G'* and yield stress make the 12% (w/w) FS-SFO a more desirable concentration.

3.2 Printing Parameter Characterization

Structures produced through e-FDM are comprised of continuous cylindrical filaments, and therefore, controlling the filament geometries is integral to ensure the fidelity of the printed structures. The simplest method to controlling filament geometry, and most importantly, the filament diameter, is to vary the extrusion flow rate and nozzle gauge. To investigate the effects of these parameters on filament diameter, single filaments printed using three flow rates (0.23, 0.52, and 0.93 mm^3/s) and three nozzle gauges (18-, 20-, and 22-gauge) were measured, and then their respective diameter ratios were calculated, as shown in Fig. 3. The diameter ratio is defined as the ratio of the filament diameter (d_f) to the inner diameter of the nozzle (d_n), where 18-, 20-, and 22-gauge nozzles possess inner diameters of 0.838, 0.603, and 0.413 mm, respectively. When a constant path speed for a 20-gauge nozzle is used, and the flow rate increases from 0.23 to 0.93 mm^3/s, the diameter ratio also increases from 0.93 ± 0.04 to 1.47 ± 0.09 (Fig. 3a). This phenomenon is caused by an under extrusion at low extrusion flow rates and an over extrusion at high flow rates. The filament diameter dependence on flow rate can be described by Eq. (2) [39] as

$$d_f = \sqrt{\frac{4Qv_p}{\pi}} \quad (2)$$

where v_p is the path speed and Q is the extrusion flow rate. Because the path speed is constant throughout testing, the extrusion flow rate is the only parameter affecting the filament

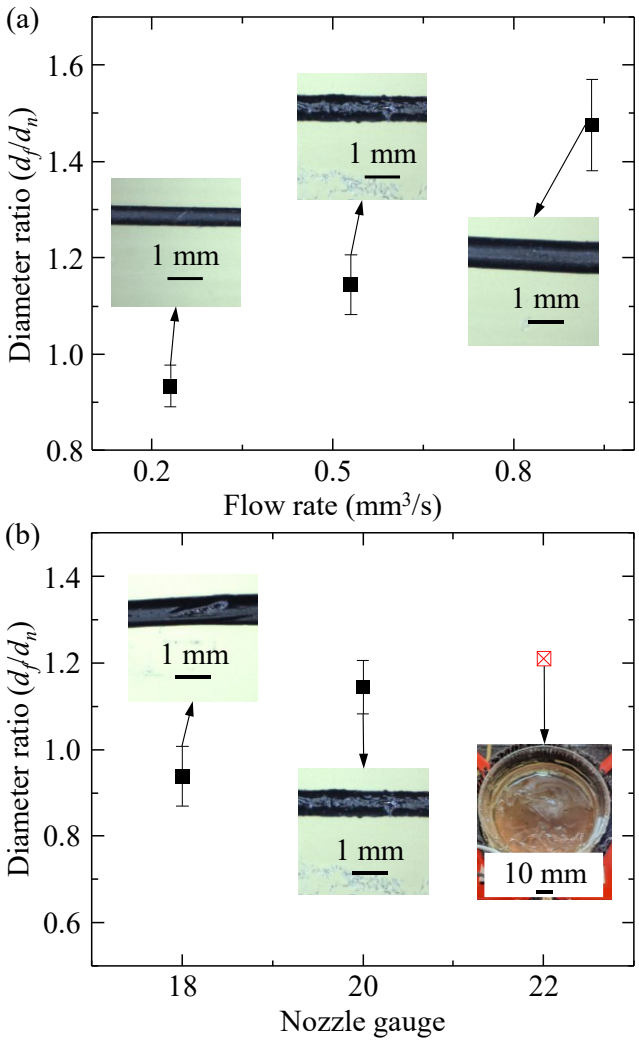

FIGURE 3: FILAMENT FORMATION IN FS-SFO SUPPORT BATH AT 85 °C. (A) FLOW RATE EFFECTS ON THE FILAMENT DIAMETER RATIO. (B) NOZZLE GAUGE EFFECTS ON THE FILAMENT DIAMETER RATIO.

diameter, and an increase in extrusion flow rate increases the filament diameter.

When the extrusion flow rate is held constant at 0.52 mm^3/s, and the nozzle gauges vary, the diameter ratios also vary, as depicted in Fig. 3b. The 18- and 20-gauge nozzles produced diameter ratios of 0.94 ± 0.07 and 1.14 ± 0.06, respectively. The 22-gauge nozzle could not extrude any PCL filament because of the increased viscous force caused by the 22-gauge's smaller inner diameter. Therefore, the 20-gauge nozzle will produce the smallest controllable filaments and allow for the highest print resolution for a PCL filament.

The controlled variations of the filament diameter through extrusion flow rate and nozzle gauge changes show that the filament produced through e-FDM is tunable. Regarding future tests, the 20-gauge nozzle and an extrusion flow rate of 0.52 mm^3/s were selected for all further e-FDM printing because they provide a controllable and repeatable filament geometry from the smallest diameter nozzle without clogging.

3.3 Surface Roughness Characterization

With a high ambient bath temperature, the dispensed PCL filament will remain molten throughout the e-FDM printing process. This allows for filaments to be dispensed with overlapping geometries when printing surfaces. Physically, the overlap ratio is defined as the ratio of the adjacent filament centerline distance (D) to the filament diameter (d_f) to measure and control the overlap between filaments. When printing structures with continuous faces, the overlap ratio will directly affect the surface roughness of the structure. Figure 4 shows the surface roughness (R_{RMS}) for single-layer PCL sheets printed with 30%, 40%, and 50% overlap ratios to be 36.1 ± 1.72 µm, 38.5 ± 2.99 µm, and 47.9 ± 5.10 µm, respectively. The R_{RMS} decreases with the overlap ratio because the proximity of the filaments printed at a lower overlap ratio reduces the air gap between the respective filaments [16, 20, 21]. Additionally, the increased temperature and molten state of the filaments increase inter-filament wetting and diffusion, resulting in an increase in neck size between adjacent filaments and a reduction of R_{RMS}. The surface roughness of PCL single-layer sheets printed via FDM was also measured and found to have a minimum R_{RMS} of 52.03 µm, proving e-FDM produces surfaces with significantly lower surface roughness when compared to FDM.

3.4 Mechanical Property Characterization

In addition to a decrease in surface roughness, e-FDM's ability to print with a lower overlap ratio should also increase the mechanical strength of the thermoplastic structures. Single-layer PCL dog bone tensile samples were printed via e-FDM and FDM to determine if e-FDM produces structures with a mechanical advantage. Material extrusion-based 3D printing methods, such as FDM, produce structures with anisometric mechanical

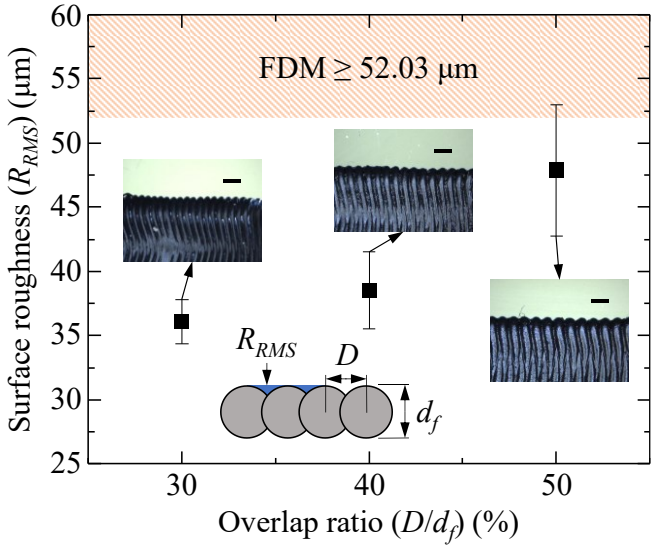

FIGURE 4: OVERLAP RATIO EFFECTS ON SURFACE ROUGHNESS. SCALE BARS: 1.0 MM

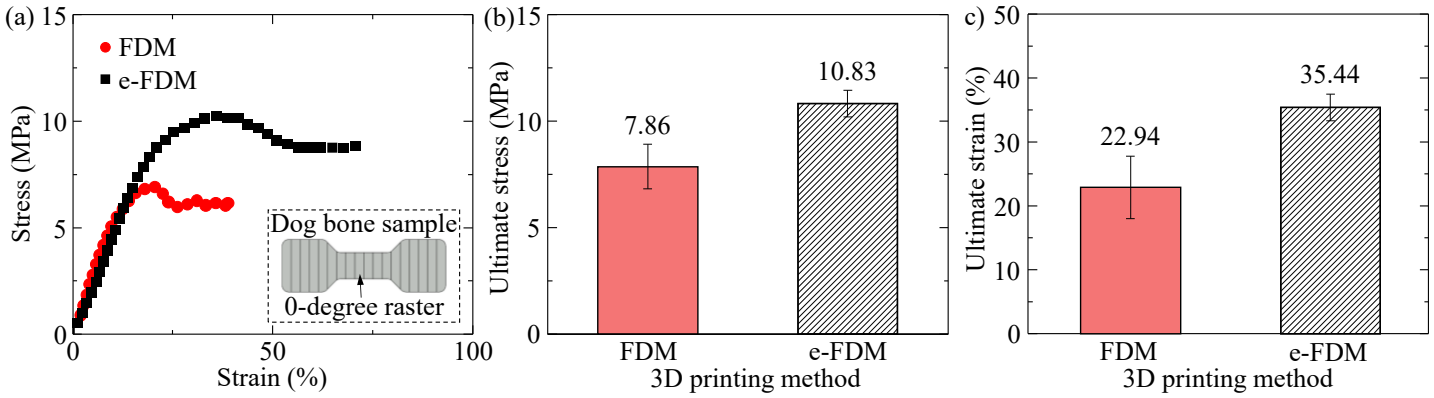

FIGURE 5: MECHANICAL PROPERTIES OF PCL DOG BONE TENSILE SAMPLES PRINTED VIA FDM AND E-FDM WITH A 0-DEGREE RASTER ANGLE. (A) STRESS-STRAIN CURVE OF FDM AND E-FDM PRINTED TENSILE SAMPLES. (B) ULTIMATE STRESS AND (C) ULTIMATE STRAIN OF FDM AND E-FDM PRINTED TENSILE SAMPLES.

properties. In the case of FDM printing, the mechanical properties parallel to the direction of the cylindrical filament axis are greater than the mechanical properties of the inter-filament bond [40, 41]. Herein, all dog bone samples were printed with a 0-degree raster angle, resulting in dog bone samples with inter-filament bonds perpendicular to the direction of tensile strain, and, therefore, the dog bone samples are printed in the weakest orientation. After printing, the average cross-sectional area of the reduced section of the dog bone samples was measured to be 7.001 ± 0.0179 mm^2 and 1.428 ± 0.094 mm^2 for e-FDM and FDM, respectively. The stress-strain curve, average ultimate strength, and average ultimate strain for the PCL dog bone samples printed using e-FDM and FDM are shown in Fig. 5. The ultimate stress and strain of the FDM dog bone samples are 7.86 ± 1.05 MPa and 22.94 ± 4.87%, while the e-FDM samples produced significantly higher values of 10.83 ± 0.62 MPa and 35.44 ± 2.11%.

The increased overlap ratio and ambient temperature of the e-FDM support bath allow for greater diffusion between adjacent molten filaments and produce larger areas of stronger physical crosslinking than FDM printed structures. This is because the temperature and size of the weld zone, the area where adjacent filaments diffuse and bond together during printing, influence the mechanical properties of the printed structure. When thermoplastics are above their glass transition temperature, polymer chains will interact and entangle, producing strengthened weld zones [42]. In FDM, the weld zone typically remains above the glass transition temperature of the filament material for approximately two seconds, resulting in limited weld time, reduced polymer diffusion and entanglement between adjacent filaments, and weak inter-filament and interlayer adhesion [42]. In e-FDM, the weld time is effectively equivalent to the printing time, and the ambient temperature is above the filaments' melting point. This produces increased polymer chain entanglement and mechanical properties in the weld zone and for the structure as a whole. Furthermore, for isothermal conditions such as e-FDM printing, the inter-filament bond strength increases with a power law dependence to weld time [43, 44] as shown in Eq. (3):

$$\sigma_b \sim \quad , \; 0.25 \le m \le 0.5 \tag{3}$$

Where σ_b is the inter-filament bond strength and t_w is the weld time. From Eq. (3), it can be deduced that the inter-filament bond strength would be significantly greater for e-FDM when compared to FDM because of the increased weld time inherent to the e-FDM technique.

3.5 Orbital Implant Simulation

Using the material properties from the mechanical testing of e-FDM, as well as average PCL density (3.16×10^{-14} g/mm^3) and Poisson's ratio (0.30) from literature [45], a numerical structural simulation of an exemplary orbital implant was performed. The patch was designed to have an overall height, width, and thickness of 27.05, 16.07, and 1.25 mm. Figure 6a depicts the orbital patch geometry and parameters of the structural simulation. The outer edge of the orbital implant was assumed to be fixed as it would be held with a medical adhesive in a procedure [46, 47]. The implant's large, flat top surface is acted on by a 35 g distributed load normal to the surface to simulate the weight of the eyeball and surrounding tissue [48, 49]. The

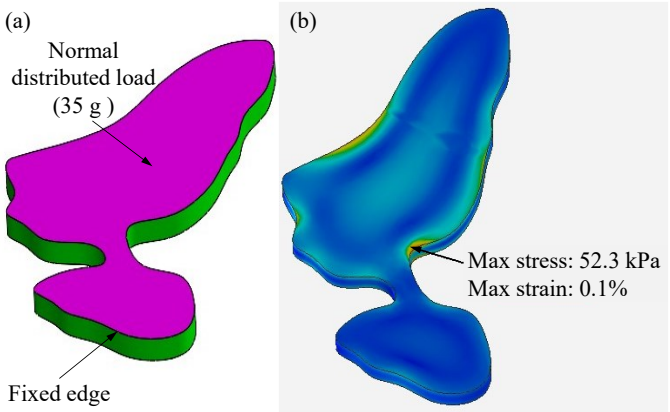

FIGURE 6: E-FDM PRINTED PCL ORBITAL IMPLANT STRUCTURAL SIMULATION. (A) SIMULATION GEOMETRY AND LOAD PARAMETERS. (B) SIMULATION RESULTS.

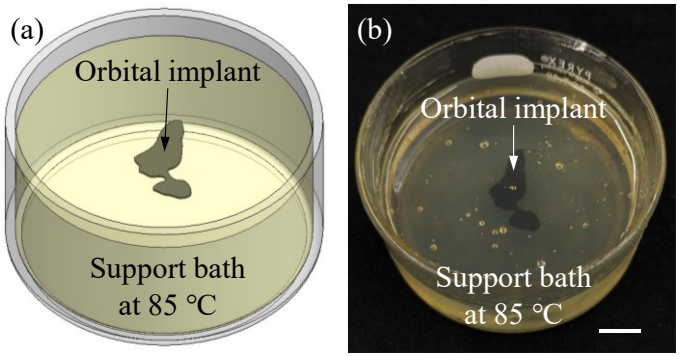

FIGURE 7: E-FDM PRINTED PCL ORBITAL IMPLANT EMBEDDED IN 85 ℃ FS-SFO SUPPORT BATH. (A) SCHEMATIC. (B) PRINTED STRUCTURE. SCALE BAR: 10.0 MM

fixed edge and loaded surface are indicated in green and pink in Fig. 6a, respectively. The simulation results are shown in Fig. 6b, where the maximum stress and strain are 52.3 kPa and 0.1%, respectively. These values are orders of magnitude lower than the ultimate stress and strain values (11.45 MPa and 36.3%) found through mechanical testing. Therefore, the simulation validates the design and mechanical properties of the e-FDM PCL orbital implant. Moreover, the increased mechanical properties produced through e-FDM should provide a more robust implant than FDM throughout the implant's degradation process, resulting in more support for the eyeball and surrounding tissue.

3.6 Orbital Implant Printing, Shape Fidelity, and Installation

After determining the viability of the orbital implant design through simulation, the exemplary orbital implant was printed via e-FDM, measured to determine shape fidelity, and implanted into a mock skull with an orbital fracture. First, the orbital implant was printed into a support bath held at 85 ℃ to ensure the PCL filament was molten throughout the printing process. Figure 7a depicts a model of the orbital implant printed into the high-temperature FS-SFO support bath, and Fig. 7b shows an image of the actual PCL orbital implant printed into said support bath. The selected support bath concentration can hold the deposited filament *in situ* at 85℃ – well above the melting temperature of PCL – allowing for greater intralayer diffusion, low surface roughness, and increased mechanical properties. After printing, the support bath and orbital implant were cooled to room temperature to allow the implant to solidify. Then, the implant was removed, cleaned of excess bath material, and measured. By comparing the height, width, and thickness of the designed and printed orbital implants, the shape fidelity of the proposed e-FDM printing technique can be validated. Figure 8a depicts the CAD model and designed height and width of the orbital implant, while Fig. 8b shows the printed PCL orbital implant and the measured respective geometries. Additionally, Table 1 provides the key dimensions of the orbital implant model and printed implant, as well as the relative error between the dimensional values. From Table 1, the largest error between the model and the measured printed orbital implant was 7% for the overall thickness. The relatively low error between the designed and printed orbital implant proves the e-FDM technique prints with a high shape fidelity.

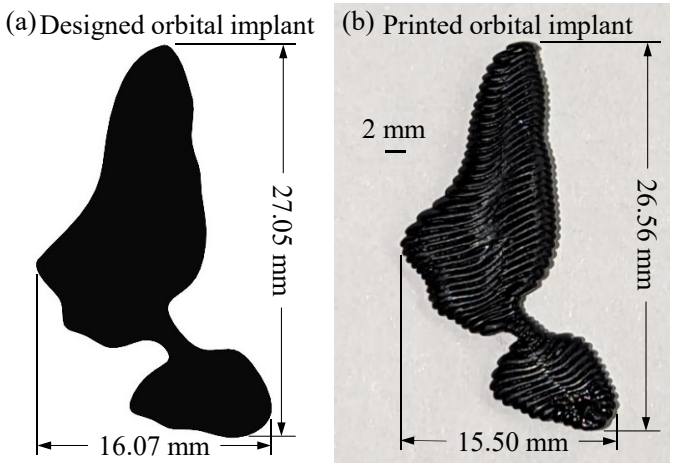

FIGURE 8: PCL ORBITAL IMPLANT MEASUREMENTS OF THE (A) MODEL AND (B) PRINTED STRUCTURE.

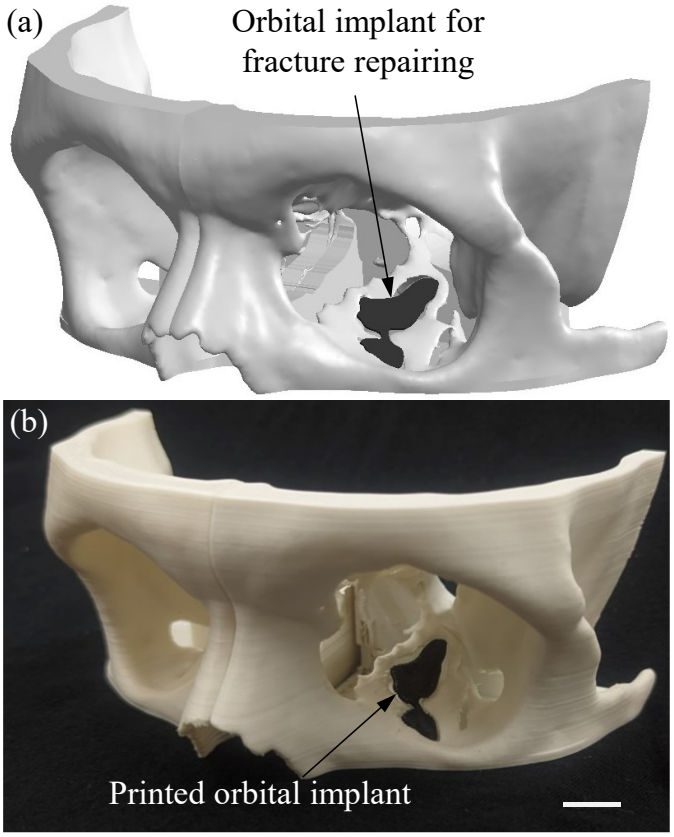

FIGURE 9: (A) SCHEMATIC OF AN ORBITAL IMPLANT INSTALLED IN THE FRACTURE SITE OF A SKULL ORBITAL. (B) PCL ORBITAL IMPLANT INSTALLED IN THE FRACTURE SITE OF A SKULL ORBITAL. SCALE BAR: 10.0MM

Additionally, the print lines on the surface of the PCL implant shown in Fig. 8b can be smoothed using an acetone bath or acetone vapor post-printing if so desired [50, 51]. Besides cosmetic effects, smoothing the surface of polymer implants can affect cell behaviors like cell attachment and migration. However, modifying the surfaces of printed PCL implants may lead to increased cell death [52, 53], and therefore, surface smoothing must be implemented only when it benefits desired cell behaviors and cell death is below an acceptable value.

After verifying the geometries, the orbital implant could be installed into a skull with an orbital fracture. Figure 9a illustrates a skull model with a bone fracture in the floor of the orbital socket as well as an implant affixed to the fracture site. The skull model used possesses an orbital fracture similar in size to fractures found in real patients. The orbital implant itself is designed to have a geometry that would fill the fracture site and have a top surface similar to the curvature of the orbital socket floor. PCL as a material is semi-flexible and, therefore, can be contoured to match the compound curves of the socket [8, 14].

TABLE 1: DESIGNED ORBITAL IMPLANT MODEL AND PRINTED ORBITAL IMPLANT DIMENSIONS WITH RELATIVE ERROR.

Dimension	Designed model	Printed implant	Relative error
Height (mm)	27.05	26.72 ± 0.13	1%
Width (mm)	16.07	15.59 ± 0.11	3%
Thickness (mm)	1.25	1.34 ± 0.06	7%

Figure 9b shows the skull with the printed PCL orbital implant within the orbital fracture. The validation of shape fidelity and implantation of the orbital implant proves the viability of e-FDM for producing patient-specific orbital implants from biodegradable thermoplastics.

4. CONCLUSION

The effectiveness of the proposed e-FDM 3D printing method has been investigated and verified. It was discovered that an increase in FS concentration increased *G'* and yield stress of the FS-SFO support bath. The filament diameter can be controlled and tuned during printing by altering the extrusion flow rate or nozzle gauge. However, filaments cannot be extruded when using a 22-gauge nozzle or smaller because of the viscous forces of PCL. The selected filament overlap ratio and the bath temperature of the melting point of the thermoplastic filament greatly enhance the surface roughness and mechanical properties of the printed structures. Additionally, structures can be created through e-FDM with significantly enhanced surface morphology and mechanical properties than structures printed via FDM. Lastly, e-FDM can produce well-defined and mechanically robust thermoplastic structures that can be used as patient-specific orbital implants.

ACKNOWLEDGEMENTS

Guangrui Chai acknowledges the support of the Liaoning Provincial Natural Science Foundation of China (2022-YGJC-27). Yifei Jin acknowledges the support of the National Science Foundation (OIA-2229004).

REFERENCES

[1] Seen, Sophia, *Craniomaxillofacial Trauma & Reconstruction*, 2021
[2] Shin, Jun Woo, *Journal of Craniofacial Surgery*, 2013
[3] Bachelet, Jean-Thomas, *Journal of Oral and Maxillofacial Surgery*, 2018
[4] Le Clerc, N, *Journal of Plastic, Reconstructive & Aesthetic Surgery*, 2020
[5] Lai, Kenneth KH, *Canadian Journal of Ophthalmology*, 2023
[6] Demir, Can İlker, *Kocaeli Medical Journal*, 2022
[7] Banica, Bogdan, *Maedica*, 2013
[8] Kim, So Young, *Journal of Cranio-Maxillofacial Surgery*, 2019
[9] Young, Stephanie M, *British Journal of Ophthalmology*, 2017
[10] Teo, Livia, *Orbit*, 2015
[11] Abd Razak, Saiful Izwan, *International Journal of Basic and Applied Sciences*, 2012
[12] Grémare, Agathe, *Journal of Biomedical Materials Research Part A*, 2018
[13] Winarso, Rochmad, *Heliyon*, 2022
[14] Kim, Jun Hyeok, *Journal of Anatomy*, 2020
[15] Yeo, Taegyun, *Journal of Industrial and Engineering Chemistry*, 2021
[16] Mitchell, Kellen, *Separation and Purification Technology*, 2023
[17] Arrigo, Rossella, *Polymers*, 2022
[18] Rajpurohit, Shilpesh R, *Rapid Prototyping Journal*, 2018
[19] Garg, Ashu, *International Journal of Mechanical Sciences*, 2017
[20] Mendricky, Radomir, *Tehnički vjesnik*, 2020
[21] Khan, MS, *Materials Today: Proceedings*, 2020
[22] Hua, Weijian, *ACS Biomaterials Science & Engineering*, 2021
[23] Friedrich, Leanne M, *Soft matter*, 2021
[24] Ding, Houzhu, *Applied Sciences*, 2018
[25] Stojkov, Gorjan, *Gels*, 2021
[26] Jin, Yifei, *ACS Applied Materials & Interfaces*, 2019
[27] Huang, Kai, *Applied Materials Today*, 2021
[28] Afghah, Ferdows, *Scientific Reports*, 2020
[29] Hua, Weijian, *Journal of Manufacturing Science and Engineering*, 2023
[30] Hua, Weijian, *ACS Applied Materials & Interfaces*, 2022
[31] Prendergast, Margaret E, *Advanced Healthcare Materials*, 2022
[32] Li, Qi, *ACS Applied Materials & Interfaces*, 2022
[33] Baptista, Cameron, *Polymer*, 2020
[34] Shahverdi, Mohammad, *Scientific Reports*, 2022
[35] Bulut, Erdim, *Journal of the American Oil Chemists' Society*, 2010

[36] Whitby, Catherine P, *Frontiers in Sustainable Food Systems*, 2020
[37] Whitby, Catherine P, *Journal of Colloid and Interface Science*, 2018
[38] Mitchell, Kellen, *Chemical Physics Reviews*, 2024
[39] Jin, Yifei, *Materials Science and Engineering: C*, 2017
[40] Khan, Saifuddin, *Materials Today: Proceedings*, 2022
[41] Peng, WANG, *Chinese Journal of Aeronautics*, 2021
[42] Seppala, Jonathan E, *Soft matter*, 2017
[43] Gao, Xia, *Additive Manufacturing*, 2021
[44] Yang, F, *Macromolecules*, 2002
[45] Narayanan, Lokesh Karthik, *Applied Sciences*, 2020
[46] Harman, Melinda, *Gels*, 2023
[47] Yang, Jae-Hyuk, *Archives of Craniofacial Surgery*, 2018
[48] Yoo, Jun Ho, *Journal of Craniofacial Surgery*, 2013
[49] Bhardwaj, Rajneesh, *Biomechanics and Modeling in Mechanobiology*, 2014
[50] Kosik-Kozioł, Alicja, *ACS Biomaterials Science & Engineering*, 2018
[51] Wang, Weiguang, *CIRP Annals*, 2020
[52] Feng, Kuan-Che, *Soft matter*, 2018
[53] Huber, Fabian, *Materials*, 2022